Synthesis and photocatalytic activity of BiOBr nanosheets with tunable exposed {0 1 0} facets

Xuyang Xiong, Liyong Ding, Qingqian Wang, Yongxiu Li, Qingqing Jiang, Juncheng Hu*

Key Laboratory of Catalysis and Materials Science of the State Ethnic Affairs Commission & Ministry of Education, South-Central University for Nationalities, Wuhan 430074, China

ARTICLE INFO

ABSTRACT

A series of BiOBr nanosheets with tunable exposing proportion of (0 1 0) facets had been synthesized. In the synthesis process, different *n*-alcohols are used, which not only promote the exposure of (0 1 0) facets, but also modulate the size and thickness of these BiOBr nanosheets in a wide range. Furthermore, these nanosheets showed an efficient photodegradation activity for salicylic acid (SA) and Rhodamine B (RhB). By comparison, the sample prepared in *n*-hexanol possessed the highest photocatalytic activity than those synthesized in *n*-butanol and methanol, respectively. This excellent photocatalytic activity was attributed to the thin lamellar thickness and the exposure of (0 1 0) facets, which facilitated the separation of photoinduced electrons and holes.

© 2016 Elsevier B.V. All rights reserved.

1. Introduction

With the consumption of fossil fuels in the past centuries, human beings are now faced with great energy crisis and environmental issues. Semiconductor photocatalysis, which could use the clean and abundant solar energy for pollutant decomposition [1], water splitting [2] and CO₂ conversion [3], has been regarded as a green and promising alternative solution to energy substitution and environmental management. Rencently, Bismuth oxyhalides (BiOX (X = F, Cl, Br, I)), especially BiOBr, had attracted considerable interests. BiOBr is a novel *p*-type semiconductor crystallized in a tetragonal matlockite structure with $[Bi_2O_2]^{2+}$ slabs interleaved by double slabs of Br ions [4]. Compared with traditional photocatalysts such as TiO₂, BiOBr materials possess wider visible-light response range, better electrical conductivity and higher quantum efficiency [5,6]. Therefore, it possesses wide applications in heavy metal removal [7], nitrogen fixation [8] and sterilization [9]. However, despite the wide use of BiOBr materials in the laboratory, the narrow range of visible-light response and the inefficient charge separation and transportation restrict its use in industrial fields [10]. Therefore, modification methods were needed to enhance the photocatalytic activity of BiOBr.

Up to date, various methods had been used, such as hierarchical nanostructures [11–13], halogen-mixing solid solutions [14]

and crystal-facet control [15]. Among them, the facets-controlled synthesis of BiOBr is worthy to be mentioned, especially synthesizing crystals with tunable exposed facets. In the past few years, BiOBr nanosheets with tunable exposed (0 0 1) facets were prepared [16]. Generally, the intra-electric field of BiOBr materials is along the [0 0 1] direction and the surface energy of (0 0 1) facets is much lower than other facets [17]. Therefore, BiOBr nanosheets with dominant exposed (0 0 1) facets possess higher photocatalytic activity and are easily prepared. Contrast to the (0 0 1) faces of BiOBr materials, the (0 1 0) facets were also of vital importance [18]. In general, (0 1 0) facets had open channel characteristics, which benefiting the injection of photoinduced electrons from dyes and possessing superior activity for indirect dye sensitization degradation under visible light [19]. However, BiOBr materials with dominant exposed (0 1 0) facets were hard to obtained due to the high surface energy [20]. Therefore, special preparation methods were needed. In previous reports, BiOBr nanosheets with dominant exposed (0 1 0) facets were synthesized by adding NaOH solution [21]. However, this synthetic method has its limitations: Adding NaOH solution will lead to a complicated synthetic process, if adding more NaOH in the preparation system, a dehalogenation effect may occur and the chemical compositions will change [22]. Particularly, changing the proportion of exposed (0 1 0) facets seems hard with this method. To the best of our knowledge, there is no report on the design and fabrication of BiOBr nanosheets with tunable exposured (0 1 0) facets just by changing the solvents.

Herein, in this study, we used a novel method to synthesize BiOBr nanosheets with tunable exposed (0 1 0) facets. The facet-

dependent photocatalytic activities of the as-obtained nanosheets are studied through the degradation of salicylic acid (SA) and Rhodamine B (RhB) under visible-light. To understand the excellent photocatalytic activity of the BiOBr materials, several factors such as morphology, specific surface area and electron transport have been studied. The thinnest nanosheets with the highest exposure ratio of (0 1 0) facets possessed the highest photocatalytic activity. Considering that the morphology and crystal facets impacted the performance of these BiOBr nanosheets, the role of solvents in the synthetic process was systematically investigated by calculation and theoretical prediction. Therefore, a "solvent-dependent" study had been used to investigate the controllable synthesis of BiOBr nanosheets and the growth of BiOBr crystals. This work provided a novel method for synthesizing photocatalysts with highly efficient photocatalytic performance.

2. Materials and methods

2.1. Materials

Bismuth nitrate pentahydrate [$Bi(NO_3)_3 \cdot 5H_2O$], acetic acid, NaBr and methanol were purchased from Sinopharm Chemical Reagent Co., Ltd. (Shanghai, P. R. China). n-butanol, n-hexanol and n-hexyl acetate were purchased from Aladdin (Shanghai, China). All of the reagents were analytical grade and used without further purification.

2.2. Sample preparation

In a typical process, 1 mmol of $Bi(NO_3)_3 \cdot 5H_2O$ was dissolved into 3 mL of acetic acid and labeled as solution A. Mean while, 1 mmol of NaBr was added into 30 mL of n-alcohol (methanol, n-butanol and n-hexanol, respectively), and labeled as solution B. The mixture were stirred and sonicated until all of the chemicals were well dispersed. Subsequently, solution B was slowly added to solution A in drops with continuous stirring and sonicating, and a white precipitate was formed during this process. Then, the mixed solution was transferred to a stainless steel vessel, which was subsequently heated to 180 °C and maintained at the temperature for 5 h. When cooling down to room temperature naturally, the obtained product was collected and washed with deionized water and ethanol several times, and finally dried in the air for further use. BiOBr samples were labeled as BiOBr (M), BiOBr (B), BiOBr (H), corresponding to the different solvent methanol, n-butanol and n-hexanol, respectively. For comparison, the sample prepared in absence of n-alcohol in solution B was referred to BiOBr (W).

2.3. Characterization

X-ray diffraction (XRD) patterns were carried out in a parallel mode ($\omega = 0.5°$, 2θ varied from 20° to 80°) using a Bruker D8 Advance X-ray diffractometer with Cu Kα radiation ($\lambda = 1.5406$ Å).

The microstructure and composition size of the samples were investigated by a SU8000 field-emission scanning electron microscope (FESEM, Hitachi, Japan) at an accelerating voltage (3–5 KV), energy dispersive spectrum (EDS) was connected to the SEM. Transmission electron microscope (TEM) and high resolution transmission electron microscopy (HRTEM) were obtained on a Tecnai G20 (FEI Co., Holland) microscope operated at an accelerating voltage of 200 kV, the sample powder was dispersed into ethanol and dropped a very dilute suspension onto a copper grid. The UV–vis diffuse reflectance spectra (UV–vis DRS) were collected with a Shimadzu UV-2550 spectrophotometer from 200 to 800 nm using $BaSO_4$ as background. X-ray photoelectron spectroscopy (XPS) measurements were performed on a VG Multilab 2000 (VG Inc.) photoelectron spectrometer using Al Kα radiation as the excitation

source. The Brunauer–Emmett–Teller (BET) specific surface areas of the samples were evaluated through the nitrogen adsorption and desorption isotherms using a Micromeritics ASAP 2020 gas adsorption apparatus (USA). Photoluminescence (PL) measurements were carried out at room temperature in a Hitachi F-7000 with a 150 W Xe lamp. The samples were excited at 300 nm, and the emission filter (300–800 nm) was used to minimize the background single at the excitation wavelength. The surface photovoltage (SPV) spectra measurement was carried out based on the lock-in amplifier. The measurement system consisted of a source of monochromatic light, a lock-in amplifier (SR830, Stanford Research Systems, Inc.) with a light chopper (SR540, Stanford Research Systems, Inc.), and a sample chamber. Salicylic acid (SA) and Rhodamine B (RhB) were chosen as the simulated pollutants to evaluate the photocatalytic activity of the as-prepared single crystalline nanosheets. The esters species after reaction were detected by an Alliance 2695 high performance liquid chromatography (HPLC) equipped with UV–vis diode array detector using a C18 inversed-phase column (Agilent Eclipse XDB-C18, 150×4.6 mm, 5 μm). Ultrapure water and methanol were used as mobile phase, the injection volumn was 10 μL and the flow rate was 1.0 mL min^{-1}.

2.4. Measurements of photocatalytic activity

The photocatalytic activity of the as-synthesized BiOBr samples was measured by the degradation of SA and RhB aqueous solution. A 350 W Xe lamp with an ultraviolet cutoff filter ($\lambda \geqq 420$ nm) was used to provide visible light. All experiments were carried out at 20 °C in an 80 mL of self-designed quartz photo-chemical reactor. The distance between the lamp and the glass reactor was about 5 cm. In each run, 50.0 mg catalyst was dispersed into 50.0 mL of RhB (20.0 mg L^{-1}) or SA (20.0 mg L^{-1}) aqueous solution. Then, the suspension was treated by ultrasonication for 10 min and stirred in dark for 1 h to ensure the establishment of the adsorption-desorption equilibrium. During the photoreaction, 5 mL of suspension was removed from the reactor at regular time intervals of 4 min and centrifuged. Finally, the concentration of catalyst-free RhB and SA solution were analyzed by the UV–vis spectrophotometer (UV-2550, Shimadzu). The active species during the photodegradation reaction were determined by dissolving 0.05 mmol trapping agents, including EDTA, $AgNO_3$, isopropanol (IPA), benzoquinone (BQ), which could capture photo-induced holes, photo-induced electrons, $^{\bullet}OH$ radical and $^{\bullet}O_2{}^-$ radical, respectively.

2.5. Theoretical calculation

The calculation for Bi^{3+} ions with CH_3COO-, $CH_3 -O-$, $CH_3-(CH_2)_3 -O-$, $CH_3-(CH_2)_5 -O-$ and H^+ ions with acetic acid and terminated oxygen on the (0 0 1) surface were performed by density functional theory (DFT) method with B3LYP, which accompanied with basis sets of a $6-31+G(d,p)$ set for H, O, C atoms and a lanl2dz set for Bi atom within the Gaussian 09 package. The $H^+ \longleftarrow HOOCCH_3$ and $H^+ \longleftarrow O–Bi$ system were optimized without any constraint in the beginning. The calculation for the H^+ systems took two forms: (I) the acetic acid coordinated to the H^+ atoms via the oxygen atom of the carbonyl ($H^+ \longleftarrow O=C$), (II) We had optimized the structure of (0 0 1) facets coordinating with H^+ and we found the binding energy of $H^+ \longleftarrow O–Bi$ was the lowest. In other words, H^+ preferred connecting with the oxygen atom of Bi-O bond during the synthetic process, thus we chose the oxygen atom of a single Bi-O bond to represent the terminated oxygen on (0 0 1) surface approximately.
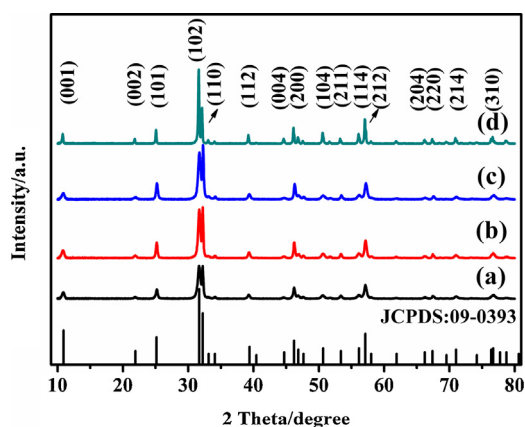
Fig. 1. XRD patterns of the samples: (a) BiOBr (M), (b) BiOBr (B), (c) BiOBr (H), (d) BiOBr (W).

3. Results and discussion

3.1. XRD and XPS

The X-ray powder diffraction (XRD) pattern of the as-prepared products was shown in Fig. 1. All of the diffraction peaks can be perfectly indexed as the tetragonal phase BiOBr (JCPDS 09–0393) with a space group of P4 and the lattice constants was about a = b = 3.96 Å, c = 8.10 Å [23–26]. Furthermore, no other diffraction peaks were detected, indicating the high purity and single-phase of the prepared samples. Compared with the sample obtain in n-alcohols, BiOBr (W) sample possessed the highest peaks. As the carbon chains of the n-alcohols increasing, the characteristic diffraction peaks corresponding to (1 0 2) and (1 1 0) facets become strong and sharp, revealing the improved crystallization of the obtained products. This could be ascribed to the electron-donating effect of the alkyl group (R-). Longer carbon chain of the alcohol solvent would be more inclined to combine with Bi^{3+} in the crystal nucleation stage, leading to lower growth rate of BiOBr nucleation and larger particles [27].

X-ray photoelectron spectroscopy (XPS) spectrum was provided to characterize the surface element composition and chemical states of the BiOBr samples (Fig. 2). No obvious impurity peaks can be detected in Fig. 2a, indicating the high purity of the BiOBr
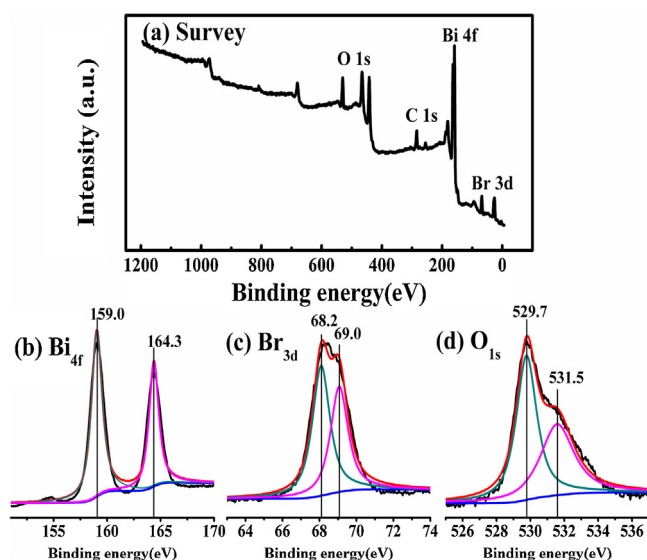
samples' surface. The two peaks centered at 164.3 and 159.0 eV, which belonged to the Bi $4f_{5/2}$ and Bi $4f_{7/2}$ respectively, indicating the main chemical states of bismuth element were tri-valence (Fig. 2b) [22]. The Br $3d_{5/2}$ and Br $3d_{3/2}$ peaks were associated with the binding energy at 68.2 and 69.0 eV, respectively (Fig. 2c). The O 1S peak could be fitted by two peaks at 529.7 and 531.5 eV, which was related to components (−OH and H_2O) absorbed on the BiOBr surface and oxygen in BiOBr (Fig. 2d). The peaks of Bi 4f, Br 3d and O 1s level were in good agreement with the previous studies [28].

3.2. Morphology

Fig. 3 shows the SEM images of BiOBr samples prepared in n-alcohols. As can be seen, all these products possessed a plate structure. The thickness of BiOBr nanosheets decreased and the size increased with the carbon chains of alcohols grew, which was in accordance with the XRD results. More interestingly, as the BiOBr nanosheets became thinner and larger, a higher exposure ratio of the top surface appeared, the detailed data are shown in Fig. S1 and Table.S1. This might ascribe to the distinguishing dissolving capacity and viscosity of different solvents [22]. Furthermore, the general morphologies of BiOBr samples are shown in Fig. S2. All these BiOBr nanosheets aggregated into microflowers. When the solvent was methanol, BiOBr (M) microflowers had the largest diameter, and the nanosheets were organized densely (Fig. S2a and b). When using n-butanol as solvent, the diameter decreased and the nanosheets became thinner and looser, besides, these thin nanosheets were more likely sticking together (Fig. S2c). Finally, BiOBr (H) sample had the smallest diameter and the thinnest nanosheets (Fig. S2d). In summary, as the carbon chains of alcohols grew, the diameters of the microflowers decreased with a looser structure, implying the sterically hindering effect of long-chain alcohol. All these detailed data are presented in Table 1. The SEM images of BiOBr sample prepared in absence of water are shown in Fig. S3. Compared with the sample synthesized in n-alcohols, BiOBr (W) possessed an irregular shapes and thick thickness (Fig. S3a and b). Besides, the magnifying image showed a rough surface of these nanosheets (Fig. S3c). The chemical composition of the as-prepared samples was also detected by EDS (Fig. S4), indicating that the BiOBr samples contained elements of O, Br and Bi.

The transmission electron microscopy (TEM) images gave more details about the interior structure of the as-prepared products. As can be seen from Fig. 4, the BiOBr samples prepared in n-alcohols indeed aggregated into microflowers (Fig. 4a and b). Moreover, HRTEM image confirmed the single crystallization nature of these BiOBr nanosheets (Fig. 4c). Since the ordered lattice fringes with an inter-planar space of 2.1 Å and 2.8 Å could be indexed as the (0 0 4) and (1 0 2) planes of tetragonal BiOBr, and the angle between them was about 45.9° (Fig. 4d), which is identical to the theoretical value of the angle between the (0 0 4) and (1 0 2) planes, these structure information indicated the BiOBr nanosheets were enclosed by dominant (0 1 0) facets [19,21]. However, the BiOBr nanosheets in absence of alcohols varied in irregular sizes and the corresponding HRTEM images showed a polycrystalline characteristic (Fig. S5). As aforementioned, the structure and morphology of BiOBr samples were deeply influenced by the alcohols.

3.3. Nitrogen adsorption-desorption isotherm

A nitrogen adsorption-desorption isotherm measurement was conducted to further investigate the structural characteristics of the BiOBr samples obtained in different solutions (Fig. 5). The sample prepared in absence of alcohols possessed small specific surface area and no pores were detected. However, BiOBr samples synthesized in n-alcohols displayed type IV adsorption-desorption isotherms with a type H3 hysteresis loop at high relative pres-
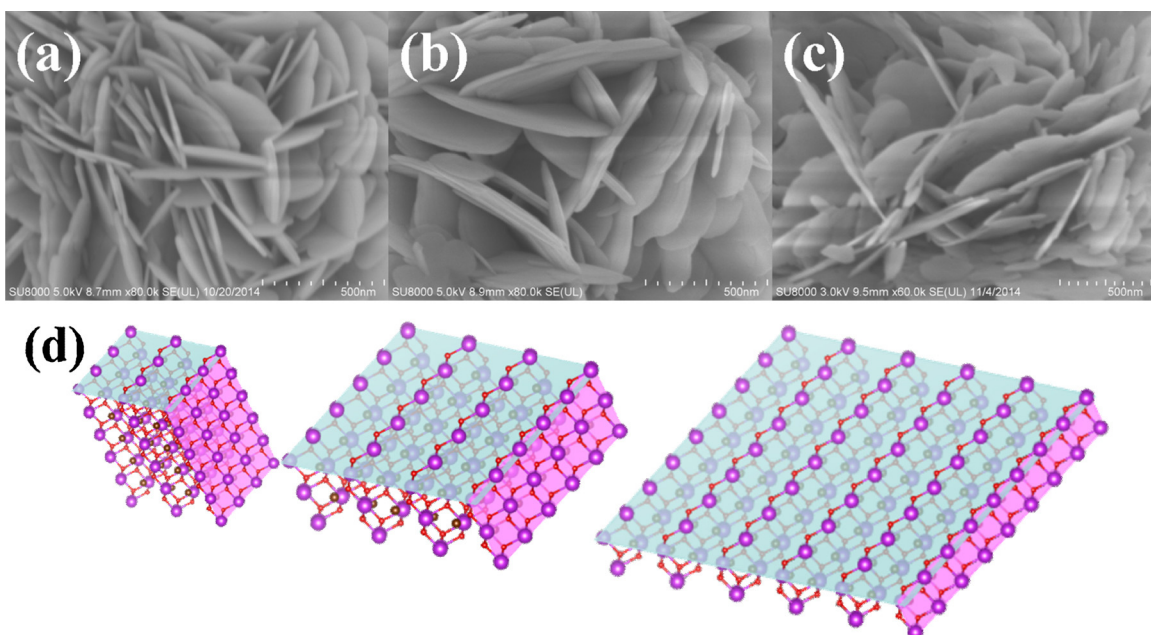

Fig. 2. XPS spectra of BiOBr samples.

Fig. 3. SEM images of BiOBr nanosheets. (a) BiOBr (M), (b) BiOBr (B), (c) BiOBr (H), (d) A schematic for the morphology transform.

sures between 0.8 and 1.0, which were typical characteristics of mesoporous materials [29]. This was also confirmed by the corresponding Barrett–Joyner–Halenda (BJH) pore diameter distribution, the small pores at about 2–3 nm could be attributed to the intervals among the intercross BiOBr nanosheets [30,31]. From Fig. 5 inset, the distance among BiOBr (H) nanosheets was larger than that in the other two samples, revealing the stronger sterically hindering effect of n-hexanol. The detailed BET specific surface areas of BiOBr samples are shown in Table 1. In summary, BiOBr (H) sample had a relatively high specific surface area.

3.4. The plausible role of solvents in morphology regulation and facets control

Based on the above observation, the plausible mechanism of BiOBr crystal growth was shown in Fig. S6. Generally, the crystal growth process contains nucleation and growth stages. At the beginning, $Bi(NO_3)_3 \cdot 5H_2O$ dissolved into acetic acid and a large number of $[Bi \longleftarrow CH_3COO]^{2+}$ ions were obtained in solution A (step 1). NaBr dissolved into n-alcohol and dissociated Br^- ions in solution B (step 2). After mixing them together and heating, the $[Bi \longleftarrow CH_3COO]^{2+}$ ions would turn into $[Bi \longleftarrow OR]^{2+}$ ions (R represents alkyl group of n-alcohol) (step 3). In order to rationalized this step, the binding energy between Bi^{3+} with CH_3COO-, CH_3-O-, $CH_3-(CH_2)_3-O-$, $CH_3-(CH_2)_5-O-$ were speculated by calculation. Generally, the binding energy could be defined as the

difference between the sum of the energies of the isolated fragments and the total energies of the combined system. As shown in Table 2, the binding energy ($\triangle E$) between Bi^{3+} and $RO-$ were negative than that between Bi^{3+} and CH_3COO-, implying step 3 was spontaneous. Moreover, considering the excess n-alcohol (n-alcohol: acetic acid = 10:1) and the high temperature (180 °C), the $[Bi \longleftarrow OR]^{2+}$ species was estimated to be the predominant species in step 4. Thus, $[Bi \longleftarrow OR]^{2+}$ ions might form as an intermediate. Moreover, $[Bi \longleftarrow OR]^{2+}$ was stable as a dense and linearly aligned structure [24]. Subsequently, the combination of Br^- ions with $[Bi \longleftarrow OR]^{2+}$ ions induced the formation of BiOBr nucleus and finally they grown into nanosheets (step 5). The chemical reactions are shown (Eqs. (1)–(5)):
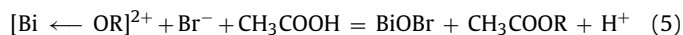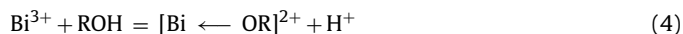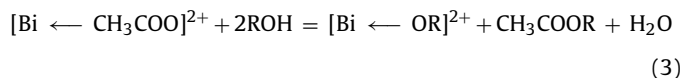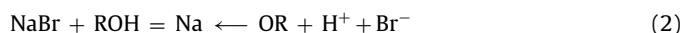
$$Bi^{3+} + CH_3COOH = [Bi \longleftarrow CH_3COO]^{2+} + H^+ \tag{1}$$

$$NaBr + ROH = Na \longleftarrow OR + H^+ + Br^- \tag{2}$$

$$[Bi \longleftarrow CH_3COO]^{2+} + 2ROH = [Bi \longleftarrow OR]^{2+} + CH_3COOR + H_2O \tag{3}$$

$$Bi^{3+} + ROH = [Bi \longleftarrow OR]^{2+} + H^+ \tag{4}$$

$$[Bi \longleftarrow OR]^{2+} + Br^- + CH_3COOH = BiOBr + CH_3COOR + H^+ \tag{5}$$
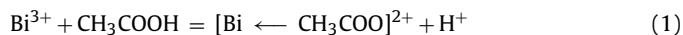
Table 1
Physicochemical property and photocatalytic activity of the BiOBr samples.

Sample	H^a (nm)	L^b (μm)	S_{BET} (m² g⁻¹)	K^c (10^{-3} min⁻¹)	K^d (10^{-2} min⁻¹)	K^e (10^{-5} g min⁻¹ m⁻²)	K^f (10^{-4} g min⁻¹ m⁻²)
BiOBr(W)	158.18	–	2.79	0.11	1.56	3.9	5.59
BiOBr(M)	26.32	3.35	7.05	0.19	6.32	2.70	8.97
BiOBr(B)	21.58	2.86	14.73	1.34	7.38	9.09	5.01
BiOBr(H)	16.46	2.5	26.78	2.35	8.86	8.78	3.31

[a] Approximate thickness (nm).
[b] Diameter of flower-like BiOBr microspheres from SEM images.
[c] The degradation rate constant of SA.
[d] The degradation rate constant of RhB.
[e] Normalized degradation rate constant of SA.
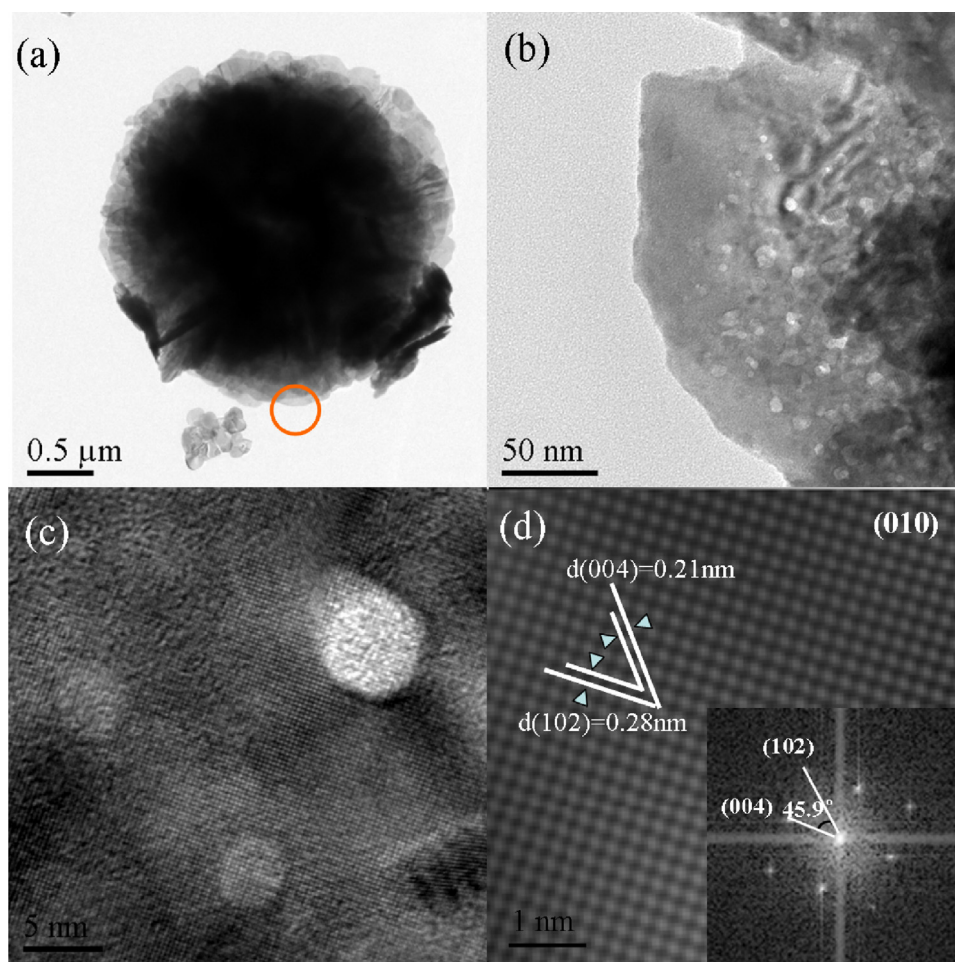[f] Normalized degradation rate constant of RhB.

Fig. 4. TEM images of BiOBr (H) nanosheets: (a) The low-magnification TEM image, (b and c) HRTEM images, (d) The corresponding magnified HRTEM image and the FFT patterns (inset).
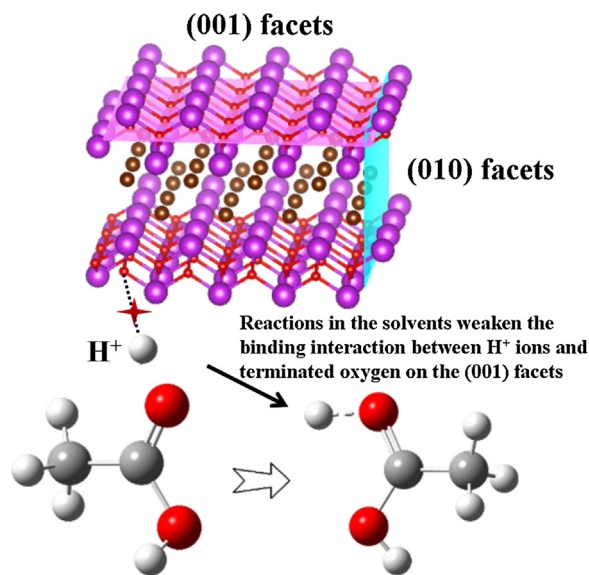
In step 5, the longer carbon chains were easier to donate their electrons, leading to stronger dipolar bonds between (R—O)$^-$ and Bi^{3+}, thus the increased carbon chains (R-) was favourable for the coordination with Bi^{3+} and further crystallization of BiOBr nanosheets. Relatively, the alcohol with shorter carbon chains had the stronger dissolving capacity, thus more crystalline nuclei would be obtained in its methanol supersaturated medium, leading to the small crystal size [27]. During the solvothermal process, BiOBr nanosheets agglomerated into BiOBr microflowers through 3D-assembly in order to reduce the interfacial energy [32,33]. At this stage, the longer carbon chains between nanosheets significantly inhibited the agglomeration, thus leading to a small diameters and a looser structure in n-hexanol [12]. When using water as the solvent, these steps were simplified and the morphology evolution had already been studied by Jiang et al. [42].

The role of solvents in facets control was also discussed. Generally, pH value was considered as the key factor to affect the dominant exposed facets. Zhang explained that during the crystal growth stage, H$^+$ ions would cap with the terminated oxygen on the (0 0 1) surface of BiOX, thus preventing the disappearance of (0 0 1) facets. Adding OH$^-$ ions could weaken the binding interaction between H$^+$ ions and terminated oxygen on the (0 0 1) surface, thus accelerating the growth of the (0 1 0) facet [19]. Superior to this, we designed a synthesis system, in which the reactions between the solvents rather than the pH value was the main reason for (0 1 0) surface exposure (Scheme 1). In our experiment, we added acetic acid during synthetic process, together with the excess n-alcohol and an extremely acid environment, H$^+$ ions were mainly used to take part in the esterification reaction, since forming protonated carboxylic acid was the first step of esterification reaction. In a word, the solvents in our synthesis system acted as "H$^+$ ions buffers", which helped us to prepare the BiOBr nanosheets with tunable exposing proportion of (0 1 0) facets successfully. In order to confirm this hypothesis, a theoretical calculation was carried out. Fig. 6 shows the binding energy of these two systems, C=O—H$^+$ was lower than Bi—O—H$^+$, indicating H$^+$ ions were favourable to coordinate with acetic acid during the synthetic process. Besides, we had also detected ester species after reaction by HPLC to further con-

Table 2
The energies of the intermediate species and the corresponding binding energy.

	Energy	Species	Energy	Species	Energy	Binding energy ($\triangle$E)
Bi^{3+}	−3.617	CH$_3$COO—	−228.543	[CH$_3$COO—Bi]$^{2+}$	−233.161	−1.000
Bi^{3+}	−3.617	CH$_3$O—	−115.116	[CH$_3$—O—Bi]$^{2+}$	−119.782	−1.050
Bi^{3+}	−3.617	CH$_3$—(CH$_2$)$_3$—O—	−233.080	[CH$_3$—(CH$_2$)$_3$—O—Bi]$^{2+}$	−237.767	−1.070
Bi^{3+}	−3.617	CH$_3$—(CH$_2$)$_5$—O—	−311.715	[CH$_3$—(CH$_2$)$_5$—O—Bi]$^{2+}$	−316.418	−1.085

(001) facets

(010) facets

H+

Reactions in the solvents weaken the binding interaction between H+ ions and terminated oxygen on the (001) facets

Scheme 1. The plausible role of solvents in facets control.

firm our hypothesis (Fig. S7). Compared with the standard *n*-hexyl acetate sample and standard *n*-hexanol sample, we found the same peaks in the solvent after reaction, implying the existence of the esterification reaction in our synthetic process. Thus, it is reasonable to conclude that the complicate reactions between the solvents was the key factor to affect the tunable exposure of (0 1 0) facets.

To sum up, solvent could affect the crystallite size, (0 1 0) facets exposure, microflowers' diameters and the growth trend of BiOBr significantly, leading to looser and smaller microflowers with thinner and larger nanosheets.

3.5. Optical properties

In order to find the impact of the morphology change on the performance, the optical properties of the BiOBr samples was investigated. The diffuse reflectance spectrum is shown in Fig. 7. As can be seen, all these samples exhibited a strong absorption at wavelengths lower than about 450 nm, implying a photo-response region between ultraviolet and a part of visible-light. Generally, the optical absorption property of photocatalyst is often closely associated with its energy gap. The energies of the band gap of BiOBr samples could be estimated by extrapolating the straight portion of $(\alpha h\upsilon)^2$ against $h\upsilon$ plot to $\alpha = 0$ based on the formula (Eqs. (6)) [25]:

$$\alpha h\upsilon = A(h\upsilon - E_g)^{1/2} \tag{6}$$

where α, h, υ, E_g, and A are absorption coefficient, Planck constant, light frequency, band gap, and a constant, respectively. The band
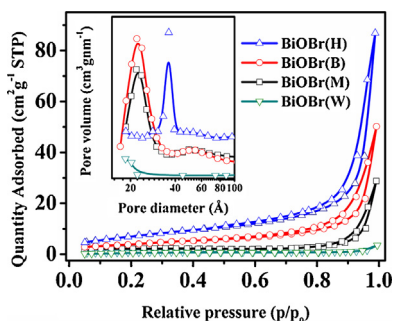

Fig. 5. Nitrogen adsorption-desorption isotherm and pore size distribution of the BiOBr samples.
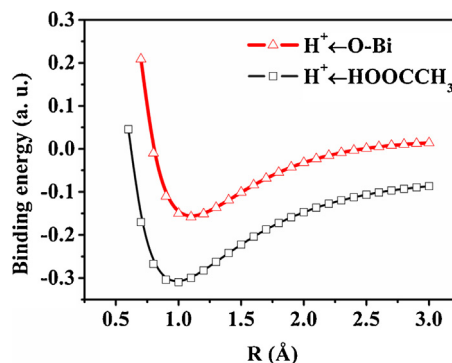

Fig. 6. Binding energies (a.u.) for H+ to acetic acid and Bi—O as functions of H—O distance in [H+—O=C] and H—O distance in [H+—O—Bi].

gap energies of these samples were estimated from 2.75–2.78 eV (Fig. 7a inset), which were comparable with those of BiOBr photocatalysts reported previously [34]. Furthermore, the BiOBr (H) sample possessed the largest band gap, and the slight differences of these samples might be attributed to the changes of building blocks and mesoporous conformation [35]. Combining with the band energies, the band edge position of these samples was theoretically predicted using Mulliken electronegativity definition (Eqs. (7) and (8)) [16]:

$$E_{VB} = X - E_e + 1/2E_g, \tag{7}$$

$$E_{CB} = E_{VB} - E_g \tag{8}$$

where E_{VB} is the valance band (VB) potential, X is the electronegativity of the semiconductor, E_e is the energy of free electrons on the hydrogen scale (≈ 4.5 eV), E_{CB} is the conduction band (CB) potential. According to the literature [16], the value of X is 6.17 eV for BiOBr. Therefore, the VB and CB levels of these samples were reasonably calculated, about 3.06 eV and 0.28 eV, respectively.

Room-temperature steady-state photoluminescence spectrum was also employed (Fig. 7b). Among these samples, BiOBr (H) sample possessed the lowest peak. This lower energy emission transfer was arisen from the indirect radiative recombination of electrons trapped at conduction band (CB) with the holes at valence band (VB). Thus, the recombination rate of photoinduced carriers was low in the BiOBr (H) sample.

To further demonstrate the photogenerated charge separation and transition properties, surface photovoltage spectroscopy and the corresponding phase spectra were carried out (Fig. 7c and d). Generally, a SPV signal starts to rise when photoinduced excess charge carriers are separated in space [36]. From the SPV spectrum, an obvious response in the ultraviolet region and a fraction of visible-light region are found, which is consisted with the former DRS observation. Besides, the strongest peak is shown in BiOBr (H) sample, revealing the efficiency separation of photoinduced holes and electrons. Considering the thinnest nanosheets of BiOBr (H) sample, it is reasonable to conclude that the photogenerated electrons could reach the surface of nanosheets easily, leading to a highly separation efficiency [35,37]. From Fig. 7d, it can be seen that the phase value of these samples are ranging from 90° to 180°, indicating negative charges accumulate at the surface of these samples [38]. In other words, the surface potential is more negative than that in the bulk as irradiating, which signifies stronger reduction ability of the sample's surface.

3.6. Photoreactivity

The photodegradation of salicylic acid (SA) and Rhodamine B (RhB) were used to evaluate the performances of different photocatalysts. Fig. 8a depicted the variation of SA concentration in
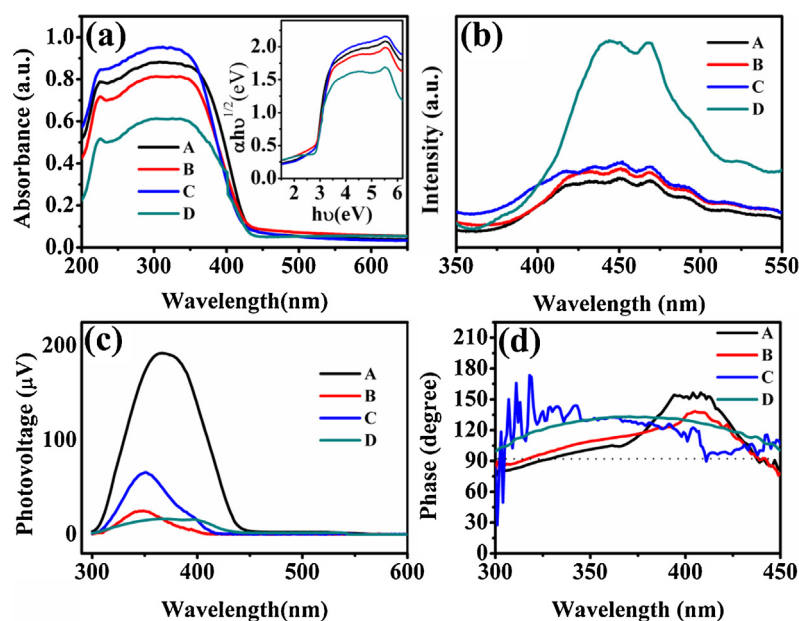
Fig. 7. (a) UV–vis diffuse reflectance spectra (DRS) of BiOBr samples. (b) Room-temperature steady-state PL spectra of BiOBr samples. (c) The SPS spectra of BiOBr samples. (d) The corresponding phase spectra of BiOBr samples. (A) BiOBr(M), (B) BiOBr(B), (C) BiOBr(H).

the presence of these three BiOBr samples under visible light irradiation. As can be seen, in the absence of catalysts, the SA self-photo-degradation was almost negligible, indicating the stronger chemical stability of SA. After 240 min, about 50% of SA degraded over BiOBr (H), while less than 30%, 20%, 10% of SA degraded in BiOBr (B), BiOBr (M) and BiOBr (W), respectively. The kinetics data of SA photodegradation was fitted well with the pseudo-first-order model (Fig. 8b). Particularly, the k value of BiOBr (H) was almost 1.8 and 21.4 times larger than that of BiOBr (B) and BiOBr (M) samples, respectively. In brief, the BiOBr (H) sample possessed the best degradation ability for SA. Considering SA was a colorless organic pollutant, which could not be sensitive under visible light irradiation, thus the degradation of SA was a direct photocatalytic process.

The photodegradation of Rhodamine B was also carried out. As can be seen from Fig. 9a, the degrading of RhB was more efficient under visible light than under UV light. Since RhB is a colorful organic contaminant, this phenomenon could attribute to the photodegradation process of Rhodamine B under visible light irradiation contained a direct photocatalytic process and an indirect dye photosensitization process, while under UV light the photosensitization process was weak. In Fig. 9b, the RhB self-photo-degradation was also negligible without adding catalysts [29,39]. Besides, RhB could be degraded completely in 32 min by BiOBr (H) sample, revealing the higher visible-light photocatalytic ability. The linear relationship between $\ln(C_t/C_0)$ and reaction time (t)

was also investigated, which demonstrated the RhB degradation reaction was pseudo-first-order model [40]. This apparent first-order rate constant was also showed in Table 1. Generally, the (0 1 0) facet of BiOBr was beneficial for the dye sensitization process, thus the BiOBr (H) sample also possessed the highest degradation rate in RhB removal. In order to determine the active species during the photodegradation process of RhB over BiOBr samples, we dissolved different trapping agents in the reaction solution before light irradiation, since the produced active species would react with the scavengers and hinder the photodegradation effect. As shown in Fig. 9c, the RhB degradation was significantly suppressed after trapping $\bullet O_2^-$ by adding BQ. When trapping photo-induced holes, electrons and $\bullet OH$ with EDTA, $AgNO_3$, IPA, respectively, the photodegradation rate exhibited much weaker restraining effect. As a result, the $\bullet O_2^-$ radical was the main active specie during the photodegradation process, which was the same as the previous work [41]. In Fig. 9d, there was no deactivation in photodegradation rates after five runs, indicating that the BiOBr samples were highly stable during the photocatalytic oxidation of the organic contaminants, which ensured its application in practical fields.

3.7. The impact factors of photoreactivity

Based on the above-mentioned experimental results, the factors for photoreactivity were discussed. Generally, the photoreactiv-
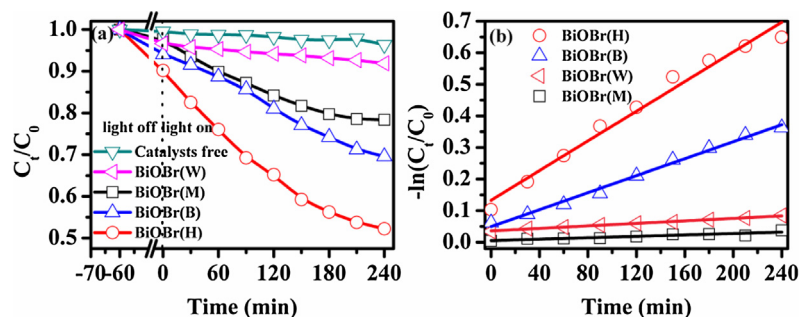

Fig. 8. UV–vis spectra of degrading salicylic acid. (a) C_t/C_0 versus time curves of salicylic acid under visible light irradiation. (b) The corresponding apparent first-order rate constant.
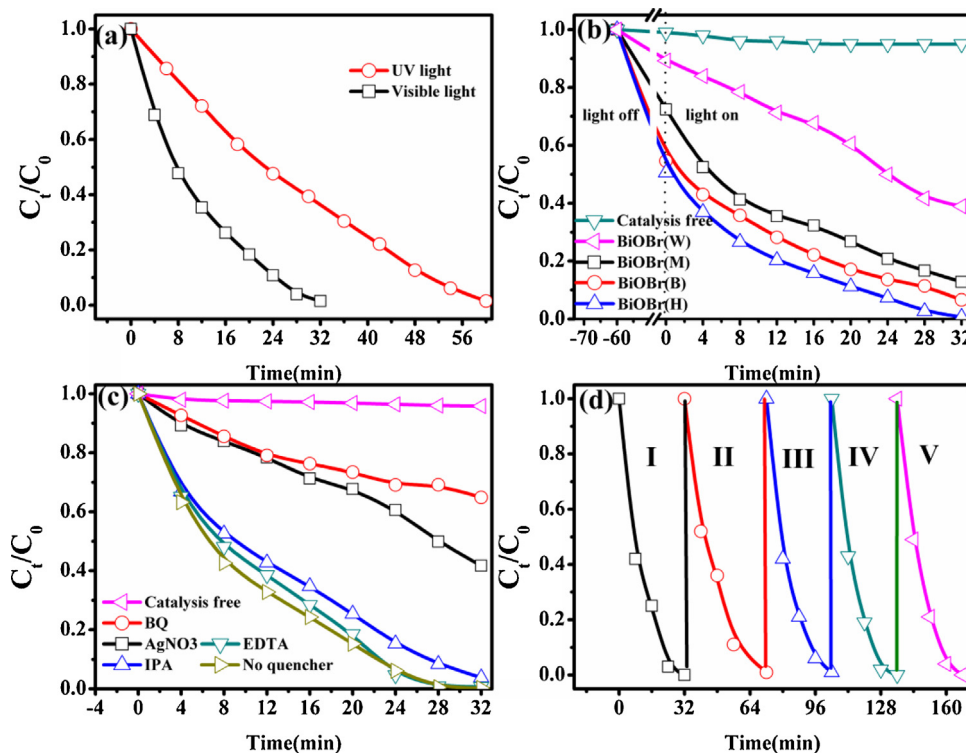
Fig. 9. UV–vis spectra of degrading RhB. (a) C_t/C_0 versus time curves of RhB under visible light and UV irradiation (BiOBr (H)). (b) Photodegradation of BiOBr samples for RhB. (c) The photocatalytic activity of BiOBr microspheres with different quenchers. (d) Recycled runs of photocatalytic degradation of RhB.

ity was influenced by its crystallinity, surficial structure, exposed facets, specific surface area and photoabsorption ability [43]. Thus, the photocatalytic ability of the sample prepared in absence of *n*-alcohols was different from that synthesized in *n*-alcohols, and the major impact factor was hard to confirm.

Considering the samples prepared in *n*-alcohols, the similar crystallinity (Fig. 1), surficial structure (Fig. 3 and Fig. S3), band gaps and visible-light absorption (Fig. 7a) indicating none of these factors causes the difference in photoreactivity. Although the (0 0 1) facets was expected as the main active facets of BiOBr materials, the effect of (0 0 1) facets should be negligible since the k increased with the increasing of (0 1 0) facets (Fig. S8). To exclude the influence of the specific surface area, the absorption properties of SA and RhB degradation were discussed (Fig. S9). As shown in Fig. S9, the adsorption ability of these samples was consistent with their specific surface area. However, when normalizing the k values of SA and RhB degradation as k^e and k^f (Table 1), k^e exhibited a slightly difference in degrading SA, implying the specific surface area was not the key factor in the direct photocatalytic process, which was consistent with previous work [43]. Interestingly, we found k^f decreased with the specific surface area increased. Considering k^f was derived from k^d and the constant of degradation rate originated from the concentration variations, the specific surface area might be an impact factor in the RhB degradation but its incidence needed further research. Apart from the specific surface area, the thickness of nanosheets was also considered as an important impact factor for reactivity in many other researches [35,44]. As shown in Fig. S10, this linear relationship illustrated the thickness of nanosheets was a key impact factor for photoreactivity in our work.

4. Conclusion

In this study, we used a novel method to synthesize BiOBr nanosheets with tunable exposed (0 1 0) facets via a simple solvothermal route. As increasing the carbon chains of the used solvents, the thickness of these nanosheets decreased while the size increased, leading to a higher exposure ratio of (0 1 0) facets. Furthermore, the diameters of these BiOBr microflowers were also influenced by the solvents. Thus, the solvents not only acted as the morphology control agent, but also as the "H+ ions buffers" in facilitating dominant (0 1 0) facets. As the morphology changed, differences among these samples appeared. The sample prepared in *n*-hexanol possessed the largest specific surface area ($26.78 \, m^2 \, g^{-1}$) among these samples. Besides, the luminescence intensity decreased while the photovoltage increased in the order of BiOBr (W), BiOBr (M), BiOBr (B), BiOBr (H). In decomposing salicylic acid, the degradation rate over BiOBr (H) sample was 1.8 and 21.4 times higher than that of BiOBr (B) and BiOBr (M) samples, respectively. As for decomposing Rhodamine B, the BiOBr (H) sample also exhibited the best photocatalytic activity. This could be ascribed as the effective separation of electrons and holes in the thinner nanosheets, and the higher exposing ratio of (0 1 0) facet benefiting the indirect dye sensitization process. Additionally, BiOBr (H) sample was stable during the recycled photocatalytic experiment, implying a potential practicability in future applications. Herein, this study not only shed light on the role of solvents in morphology modification and crystal regulation, but also provided a novel way for designing highly efficient photocatalysts.

Appendix A. Supplementary data

Supplementary data associated with this article can be found, in the online version, at http://dx.doi.org/10.1016/j.apcatb.2016.02.018.

References

[1] M.R. Hoffmann, S.T. Martin, W. Choi, D.W. Bahnemannt, Chem. Rev. 95 (1995) 69–96.
[2] A. Kudo, Y. Miseki, Chem. Soc. Rev. 38 (2009) 253–278.
[3] S.C. Roy, O.K. Varghese, M. Paulose, C.A. Grimes, ACS Nano 4 (2010) 1259–1278.
[4] F.T. Li, J.R. Ran, M. Jaroniec, S.Z. Qiao, Nanoscale 7 (2015) 17590–17610.
[5] H.J. Zhang, G.H. Chen, D.W. Bahnemann, J. Mater. Chem. 19 (2009) 5089–5121.
[6] R. Su, R. Bechstein, J. Kibsgaard, R.T. Vang, F. Besenbacher, J. Mater. Chem. 22 (2012) 23755–23758.
[7] G.F. Li, F. Qin, H. Yang, Z. Lu, H.Z. Sun, R. Chen, Eur. J. Inorg. Chem. 15 (2012) 2508–2513.
[8] H. Li, J. Shang, Z.H. Ai, L.Z. Zhang, J. Am. Chem. Soc. 137 (2015) 6393–6399.
[9] D. Wu, B. Wang, W. Wang, T.C. An, G.Y. Li, T.W. Ng, H.Y. Yip, C.M. Xiong, H.K. Lee, P.K. Wong, J. Mater. Chem. A 3 (2015) 15148–15155.
[10] J. Chen, M.L. Guan, W.Z. Cai, J.J. Guo, C. Xiao, G.K. Zhang, Phys. Chem. Chem. Phys. 16 (2014) 20909–20914.
[11] H. Gnayem, Y. Sasson, ACS Catal. 3 (2013) 186–191.
[12] L. Ding, R. Wei, H. Chen, J. Hu, J. Li, Appl. Catal. B: Environ. 172–173 (2015) 91–99.
[13] L. Ding, H. Chen, Q. Wang, T. Zhou, Q. Jiang, Y. Yuan, J. Li, J. Hu, Chem. Commun. 52 (2016) 994–997.
[14] W.D. Wang, F.Q. Huang, X.P. Lin, Scr. Mater. 56 (2007) 669–672.
[15] L. Ye, L. Zan, L. Tian, T. Peng, J. Zhang, Chem. Commun. 47 (2011) 6951–6953.
[16] D. Zhang, J. Li, Q.G. Wang, Q.S. Wu, J. Mater. Chem. A 1 (2013) 8622–8629.
[17] L. Zhao, X. Zhang, C. Fan, Z. Liang, P. Han, Phys. B (Amsterdam Neth.) 407 (2012) 3364–3370.
[18] K. Zhao, L.Z. Zhang, J.J. Wang, Q.X. Li, W.W. He, J.J. Yin, J. Am. Chem. Soc. 135 (2013) 15750–15753.
[19] J. Jiang, K. Zhao, X.Y. Xiao, L.Z. Zhang, J. Am. Chem. Soc. 134 (2012) 4473–4476.
[20] L.Q. Ye, Y.R. Su, X.L. Jin, H.Q. Xie, C. Zhang, Environ. Sci.: Nano 1 (2014) 90–112.
[21] W.W. Lin, X. Wang, Y.H. Wang, J.Y. Zhang, Z. Lin, B.T. Zhang, F. Huang, Chem. Commun. (2014), http://dx.doi.org/10.1039/C3CC41498A.
[22] J. Li, Y. Yu, L.Z. Zhang, Nanoscale 6 (2014) 8473–8488.
[23] Y.C. Feng, L. Li, J.W. Li, J.F. Wang, L. Liu, J. Hazard. Mater. 192 (2011) 538–544.
[24] L. Chen, R. Huang, M. Xiong, Q. Yuan, J. He, J. Jia, M.Y. Tao, S.L. Luo, C.T. Au, S.F. Yin, Inorg. Chem. 52 (2013) 11118–11125.
[25] C.H. Deng, H.M. Guan, Mater. Lett. 107 (2013) 119–122.
[26] S.Y. Song, W. Gao, X. Wang, X.Y. Li, D.P. Liu, Y. Xing, H.J. Zhang, Dalton Trans. 41 (2012) 10472–10476.
[27] L.P. Zhu, G.H. Liao, N.C. Bing, L.L. Wang, Y. Yang, H.Y. Xie, CrystEngComm 12 (2010) 3791–3796.
[28] Y.N. Huo, J. Zhang, M. Miao, Y. Jin, Appl. Catal. B: Environ. 111 (2012) 334–341.
[29] J.X. Xia, S. Yin, H.M. Li, H. Xu, Y.S. Yan, Q. Zhang, Langmuir 27 (2011) 1200–1206.
[30] K.S.W. Sing, D.H. Everett, R.A.W. Haul, L. Moscou, R.A. Pierotti, J. Rouquerol, T. Siemieniewska, Pure. Appl. Chem. 57 (1985) 603–619.
[31] D.V. Bavykin, V.N. Parmon, A.A. Lapkin, F.C. Walsh, J. Mater. Chem. 14 (2004) 3370–3377.
[32] M. Shang, W.Z. Wang, L. Zhang, J. Hazard. Mater. 167 (2009) 803–809.
[33] C.Y. Christopher, H.C. Zeng, J. Mater. Chem. A 2 (2014) 4843–4851.
[34] J. Henle, P. Simon, A. Frenzel, S. Scholz, S. Kaskel, Chem. Mater. 19 (2007) 366–373.
[35] Z.Q. He, Y.Q. Shi, C. Gao, L.N. Wen, J.M. Chen, S. Song, J. Phys. Chem. C 118 (2014) 389–398.
[36] I. Mora-Sero, T. Dittrich, A. Belaidi, G. Garcia-Belmonte, J. Bisquert, J. Phys. Chem. B 109 (2005) 14932–14938.
[37] Z. Zhang, C.C. Wang, R. Zakaria, J.Y. Ying, J. Phys. Chem. B 102 (1998) 10871–10878.
[38] D. Gross, I. Mora-Sero, T. Dittrich, A. Belaidi, C. Mauser, A.J. Houtepen, E. Da Como, A.L. Rogach, J. Feldmann, J. Am. Chem. Soc. 132 (2010) 5981–5983.
[39] S. Ye, L.G. Qiu, Y.P. Yuan, Y.J. Zhu, J. Xia, J.F. Zhu, J. Mater. Chem. A 1 (2013) 3008–3015.
[40] H.P. Li, J.Y. Liu, X.F. Liang, W.G. Hou, X.T. Tao, J. Mater. Chem. A 2 (2014) 8926–8932.
[41] Z.C. Liu, B.T. Wu, J.N. Niu, X. Huang, Y.B. Zhu, Appl. Surf. Sci. 288 (2014) 369–372.
[42] Z. Jiang, F. Yang, G.D. Yang, L. Kong, M.O. Jones, T.C. Xiao, P.P. Edwards, J. Photochem. Photobiol. A: Chem 212 (2010) 8–13.
[43] H.P. Li, T.X. Hu, J.Q. Liu, S. Song, N. Du, R.J. Zhang, W.G. Hou, Appl. Catal. B: Environ. 182 (2016) 431–438.
[44] X. Zhang, B.H. Li, J.L. Wang, Y. Yuan, Q.J. Zhang, Z.Z. Gao, L.M. Liu, L. Chen, Phys. Chem. Chem. Phys. 16 (2014) 25854–25861.